Exploring structure dependencies of gas-surface interactions with curved single crystals

Auras, S.V.

3

SURFACE STRUCTURE CHARACTERIZATION OF A CURVED PT CRYSTAL WITH HIGHLY KINKED STEPS

Chemical reaction steps at surfaces e.g. in heterogeneous catalysis and astronomy, are often dominated by the presence of defects rather than high-symmetry planes. However, in surface science, these processes are frequently studied by atomically flat model surfaces. Stepped surfaces provide an approach to model line defects on particles. Curved single crystal surfaces provide a useful tool for studying the influence of these defects systematically. The influence of other types of defects, such as kinks or dislocations, has received less attention.

Here, we employ a curved Pt crystal oriented such that highly kinked step edges with {210} orientation are exposed. We characterize the continuous surface structure from (111) at the apex to (432) at the sides of the apex by Scanning Tunneling Microscopy and Low Energy Electron Diffraction. Observations are analyzed in regards to their microscopic and macroscopic structure and compared to the ideal crystallographic structure. Knowing the structure of the kinked surfaces on this crystal allows us to then determine site-specific reactivities in Chapters 4 and 5.

3.1. INTRODUCTION

THE SABATIER PRINCIPLE in heterogeneous catalysis states that a good catalyst should bind reactants and reaction intermediates neither too strongly nor too weakly, in order to promote the elementary reaction steps on a catalysts surface, e.g. adsorption, dissociation, diffusion, recombination, and desorption. This can be visualized in so-called 'volcano plots', where the catalytic activity of different materials is plotted against their adsorption energies towards specific reactants. The name-giving volcano form illustrates that peak catalytic performance is typically found at intermediate binding strengths. For a number of heterogeneously catalyzed reactions, Pt has been found to be an exceptionally well-suited catalyst, at or near the top of volcano plots. For example, the three-way catalyst built into car exhausts makes use of the catalytic performance of Pt towards CO oxidation, hydrocarbon oxidation, and NO_x reduction, all under the same reaction conditions. Moreover, CO oxidation on well-defined Pt(111) surfaces is one a standard system used to study all fundamental aspects of surface reactions. As the reaction follows the Langmuir-Hinshelwood mechanism, it is an example for a typical catalytic surface reaction involving several reactions steps, causing complex reaction dynamics.[1–4] The simplest reaction of the smallest molecule, hydrogen dissociation, also takes place readily on Pt(111) surfaces. Beyond its relevance industrial processes, this system is of central importance to the development of models in gas-surface dynamics and electrochemisty.[5, 6]

While reactions on high-symmetry faces are still most frequently studied in surface science, chemical reactivity on catalytic Pt surfaces is often improved by the presence of lower-coordinated sites, such as steps, kinks, and other surface defects.[7–12] Recently, even step-type and step density effects on chemical reactions have been observed.[13–16] In the case of nanoparticles, which are commonly deposited on an oxide support in industrial applications, lower-coordinated sites (edges, corners, as well as steps and kinks) may actually comprise a majority portion of the exposed surface.[17–19]

Line defects, i.e. steps on high-symmetry terraces, are among the more frequently studied defect sites, yet kink sites may increase chemical reactivity compared to close-packed steps.[20, 21] They can also cause different step-step interactions, thus influencing surface structure.[22–25] However, only few studies investigate the influence of kinks on catalytic reactions on Pt surfaces [14, 26, 27]

As kinked steps on (111) terraces of *fcc* metals are comprised of variable ratios of A- and B-type line segements ({001} and {110} microfacets), they are also inherently chiral and open possibilities to study enantioselective reactions.[28, 29] Chiral metal surfaces provide a way to introduce chirality to heterogeneous catalysis in a way that is stable at harsher environments used in industrial catalysis. Several examples of enan-

tioselective adsorption on chiral Cu surfaces have been identified,[30–34] as well as enantioselective decomposition reactions.[35, 36] Studies also point towards the potential of chiral chemistry on kinked Pt surfaces.[37–41]

In this context, curved crystals with varying surface structure offer the potential to study even small effects of surface defects. However, to unravel the influence of different surface sites, the changing surface structure must be characterized across the entire range of curvature of such samples. This is particularly important for the curved Pt crystal with kinked step edges we present here. It features surfaces of both chiralities, with varying compositions of (111) terraces, steps (from {001} and {110} microfacets), and kinks. This chapter aims to thoroughly characterize the surface structures found across the crystal, which is crucial to the interpretation of results reagrding chemical reactivity of achiral (chapters 4 and 5) molecules, as well as future adsorption experiments involving chiral organic molecules.

3.2. CRYSTALLOGRAPHIC ORIENTATION

Platinum crystallizes in the face-centered cubic (*fcc*) crystal structure. Its lattice can be described by three translational vectors. Surface terminations of the bulk lattice can be described by Miller indices (*hkl*) or the corresponding vector along the surface normal [*hkl*].

The curved crystal described here, shown in figure 3.1a), is cut from a Pt bulk single crystal. It can be seen as a slice of a cylinder with a rotational axis axis along the [11$\bar{2}$] vector, oriented such that at the apex (111) is exposed, as figure 3.1b) demonstrates. Due to the macroscopic curvature of the crystal, at the sides surfaces with an increasing 'miscut' angle are exposed. The entire crystal surface curves across 31°, causing surface structures to range from surfaces with (111) terraces that extend hundreds of nanometers to surfaces with terraces of less than a nanometer. Figure 3.1c) plots expected terrace widths and step densities along the curved surface. It therefore can be described as *c*-Pt(111)[11$\bar{2}$]-31°, according the nomenclature introduced in chapter 2. These surfaces exhibit {210}-oriented steps, i.e. steps with an orientation halfway in between {001}/A-type steps and {110}/B-type steps.[1] As a result, these {210} steps feature inner and outer kinks separating segments of A- and B-type steps. Surface atoms at a kink site are less coordinated by other surface atoms than they would be as part of a terrace or a straight step edge. They are thus often assumed to be more active towards adsorption and chemical reactions.

In figure 3.1d) we draw two surfaces with {210} steps. The atoms at the top edge illustrate how segments can be described as A- (blue) or B-type (red). There, segments are only one atom long, resulting in a maximum density of kinks along the

[1] We use Miller indices {hkl} to indicate the set of equivalent surfaces.

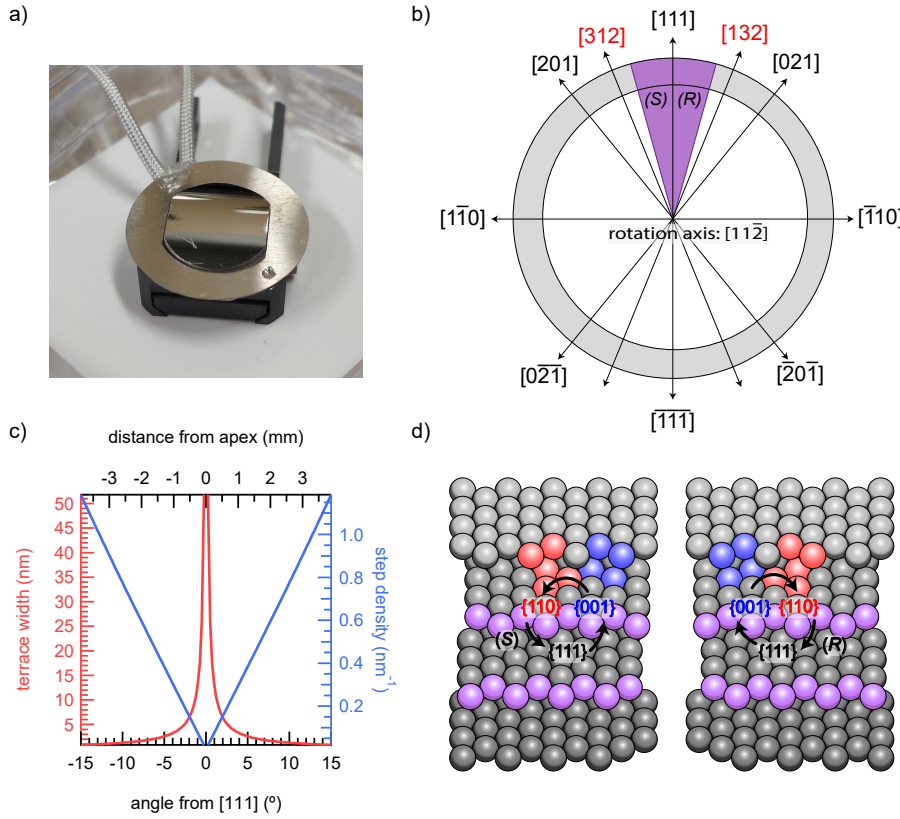

Figure 3.1: a) Photo of the curved Pt crystal. b) Depiction of crystallographic orientations along the surface of a cylinder with its rotational axis along [11$\bar{2}$] of a *fcc* crystal. The crystallographic range of the crystal sample displayed here is indicated in purple. As the surface curves away from the (111) apex, steps with [201] or [021] orientation are introduced on each side to accommodate the macroscopic curvature. The hollow sites at the step edge have *(S)* or *(R)* chirality respectively. c) Expected terrace widths (red) and step densities (blue) along the curved Pt single-crystalline surface with (111) at the apex. d) (423)$^{(S)}$ and (243)$^{(R)}$ surfaces that can be found to either side of the crystal. At the top step edge is illustrated how the kinked {210}-oriented step edges can be seen as consisting of small segments of {001}/A- and {110}/B-type steps. The middle step edge illustrates how the chirality is determined at the hollow site of the step edge. The (423) surface on the left has step edges with *(S)* chirality, the (243) surface on the right has step edges with *(R)* chirality.

step edge. However, the same crystallographic orientation/ Miller indices can also be maintained if the step edge forms longer facets and thereby reduces the amount of kinks, as long as the overall lengths of A- and B-type facets remain equal. Causes can be thermal roughening or reconstruction. Simulations of a kinked Pt(643) surface show a reduced kink density at elevated temperature.[38, 39] Characterizing the structure of these kinds of surfaces in regards to their kink density is thus crucial in order to interpret the results of subsequent experiments. Furthermore, it has to be determined if the kink density changes across the crystal from low to high step density.

Compared to straight steps, the kinked steps on this curved Pt crystal reduce surface symmetry due to the introduction of two separate microfacets. As a result, surfaces found at the two sides of the crystal are chiral to each other at the same angles from the apex. Figure 3.1d) depicts two {432} surfaces with opposite chirality, the (423) and (243) surfaces respectively. With the middle step edge we illustrate how the chirality of the surface is determined.[31, 41] Looking from above onto the hollow site of the step edge, three microfacets surround the inner corner: {110} and {001} facets along the step and a (111) terrace. Going from {001} to {110} to (111) will then result in a right-handed or left-handed turn. The surfaces are described as *(R)* (Latin *"rectus"*) or *(S)* (Latin *"sinister"*) chiral surfaces respectively.

For reactions involving only achiral reactants and products, no difference should be observed between *(R)*- and *(S)*-kinked surfaces. However, there may be steric advantages of one chirality when chiral molecules are part of a surface reaction. Indeed, the chirality of kinks on Pt surfaces has been shown to influence reactivity for chiral molecules, e.g. in the case of glucose oxidation. [41, 42]

3.3. SURFACE CLEANLINESS AND AVERAGE TERRACE WIDTH

The cleaning procedures employed for this Pt crystal and their implications on surface structure are detailed in chapter 5. After repeated cleaning cycles, Auger Electron Spectroscopy (AES) is employed to confirm the absence of contamination on the Pt surface. Exemplary spectra are plotted in figure 3.2 and show no significant peaks from elements other than Pt.

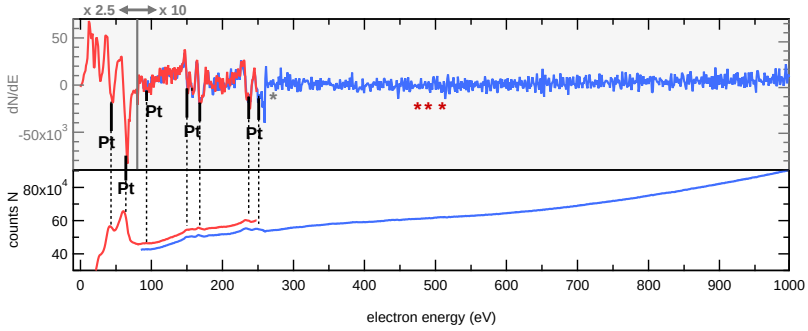

Figure 3.2: Typical Auger electron spectra of the Pt surface after cleaning. Black lines represent literature values of the most prominent dN/dE features for Pt.[43] Asterisks (*) mark most prominent features one would find in the presence of C (grey) or O (red). Spectra were recorded in several locations on the Pt surface, spanning the height and width of our sample, to ensure complete cleaning.

Subsequently, LEED is used to examine the regular ordering of the surface and check for possible surface reconstructions, step doubling, or faceting. The more ordered a surface is, the sharper the observed diffraction spots will appear. While a hexag-

onal diffraction pattern should be observed for the flat (111) surface, the diffraction spots will appear split at regularly stepped surfaces. The direction and extent of the spot splitting gives information about the average terrace width and step directions, see chapter 2. Streaking in the spot splitting would indicate wide variations in terrace widths. Figure 3.3 shows LEED patterns at the (111) apex as well as the sides of the crystal. At the center of the crystal (figure 3.3, middle of top row), we observe the reciprocal spots of a *fcc* (111) surface where the center spot is hidden behind the electron beam. Along the curvature of the crystal, we observe spot splitting which increases proportionally with the angle of curvature.

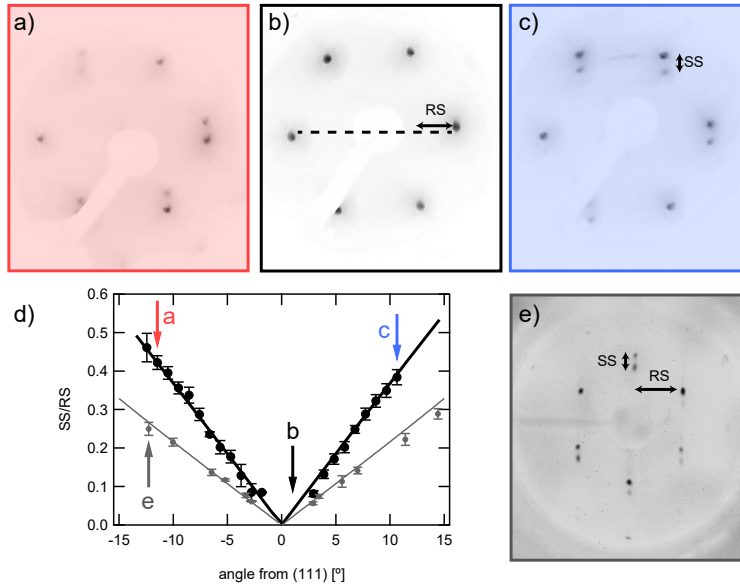

Figure 3.3: LEED patterns from different parts of the curved Pt crystal. a) - c) While around the apex a hexagonal diffraction pattern with well-defined spots is observed (b), to the sides the regular step arrays cause spot splitting (a&c). d) Spot splitting over row spacing ratios (SS/RS) along the crystal curvature. The black lines indicate expected ss/rs ratios, according to the terrace widths caused by the miscut angle from (111), see equation2. e) Demonstrates spot splitting on a similar curved crystal with close-packed steps. Both types of crystals are employed in chapter 4. Spot splitting to row spacing across the entire surface of this second crystal are added to the graph in d) in grey.

Figures 3.3a) and c) show spot splitting oriented perpendicular to the flat side of the hexagonal pattern, indicating steps along the $[11\bar{2}]$ vector, i.e. kinked {210}-oriented steps. In the case of straight A- or B-type steps, spot splitting would appear 30 ° rotated relative to the hexagon, as depicted in figure 3.3e). Figure 3.3 also plots spot splitting (SS) over row spacing (RS) ratios across the crystal. They match well with the expected ratios for monoatomically stepped surfaces at the corresponding angles away from (111), as obtained from table 2.1, confirming the expected average terrace width and the absence of reconstructions or faceting.

3.4. TERRACE WIDTH DISTRIBUTIONS

3.4.1. STEP-STEP INTERACTIONS AND THEIR IMPACT ON TERRACE WIDTH DISTRIBUTIONS

While the average terrace width can be determined by LEED at various positions of the curved surface, the microscopic structure may exhibit local variations, e.g. variations in terrace width, or deviations from the ideal step direction. These effects can be much more directly investigated by STM.

In general, step-step interactions on vicinal metal surfaces can be described via two universal effects. At short length scales, elastic repulsion between the dipoles at step edges forces steps into regular arrays to lower the free energy. This is a low entropy state.[44] Meandering of steps increases entropy in a stepped surface, and this effect dominates at larger step-step distances (d), as dipole interactions decrease with $1/d^2$.[44] Meandering, however, is limited by the fact that two steps can never cross one another.

In addition to the dipole and entropic interactions, a third effect can emerge due to the electronic band structure at the surface, at short step-step distances. This can be described by quantum confinement of electrons between the steps. Steps act as potential barriers, imposing boundary conditions to the wavefunction of the surface electrons, similar to the quantum mechanical description of a particle in a box. As a consequence, step-step distances where the electronic wavefunction forms a standing wave (eigenstates) can become favorable. For a metal, these distances correspond to multiple integers of half the Fermi wavelength ($\lambda_F/2$). This phenomenon, however, is only relevant if surface electrons can be decoupled from the band structure of the bulk, and form an independent surface states where they can behave as nearly free electrons. This condition, also called Shockley or Tamm state, is fulfilled for surfaces of Cu, Ag, and Au and is also what causes the so-called Friedel oscillations, which are spatial oscillations of the charge density. Friedel oscillations are observable when a wavefunction is reflected from a defect. Line defects, i.e. steps, can lead to similar charge density modulations. The question is whether electronic surface states can in turn shape the distribution of surface atoms. In the particle in a box analogy, this would be equivalent to the particle shrinking/expanding the boundaries of the box. Aligning the steps to match integers of the half wavelength of the surface electrons allows their wavefunction to form a standing wave, i.e. a lower state. While one might expect this to be a small energetic effect compared to the mentioned dipole and entropic interactions, a preference for 'magic' step-step distances has actually been observed on Ag surfaces with small terrace widths. With increasing terrace width, a clear transition in terrace width distributions was found.[22]

For Pt, no such clear *sp*-type surface state exists. However, surface resonances do. These do not fall into the energy gap of the bulk band structure. Specifically, a *sp* de-

rived surface resonance near the Fermi level has been shown to influence physisorption on Pt(111).[45] Quantum size effects to the conductance were found during the growth of thin layers of Pt, indicating an interaction between electronic and structural properties.[46]

For a stepped Pt surfaces with straight A- and B-type step edges a transition from the 'elastic regime' governing narrow terraces to the 'entropic repulsion' dominant at wider terraces was found to occur around 4 nm, marked by the terrace width distributions becoming wider and more asymmetric.[47] However, no quantum wells were indicated in the terrace width distributions.

Here we investigate the effects of step-step-interactions on the curved Pt crystal with kinked step edges. We investigate whether a similar transition between predominantly elastic interactions to entropic meandering can be observed for arrays with highly kinked step edges, and whether an influence of quantum size effects can be observed.

3.4.2. RESULTS OF TERRACE WIDTH ANALYSIS

We use the IGOR PRO software to analyze our STM images from various places on the crystal. The procedure can be found in Appendix D. In short, we take line profiles of the image perpendicular to the step direction given by the crystal's curvature. Finding minima along the line profile gives us the locations of the lower step edges. Terrace widths (w) are then determined pixel by pixel as distances between lower step edges. We find our terrace width distributions by sorting terrace width data in histograms. The bin width is 1/2 of the atom-atom distance (0.277 nm). The choice of our bins is due to the fact that in the case of the {210} steps, terrace width can take both full and half-integers of the interatomic distance, as figure 3.4 shows. We can determine width distributions by terrace as well as the overall distribution of all terraces in the array shown in the image.

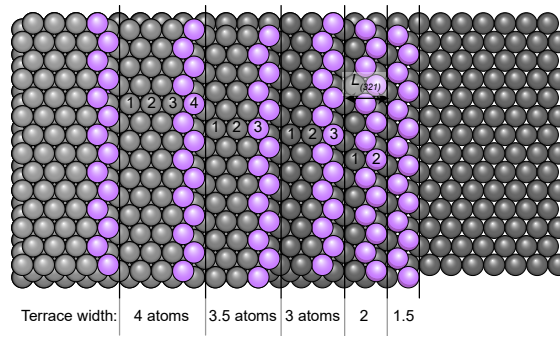

Figure 3.4: Possible terrace widths on the kinked surfaces in full and half-integer atom rows. Stepping down from the topmost step edge on the left, terraces with lengths of 4, 3.5, 3, 2, and 1.5 atom follow.

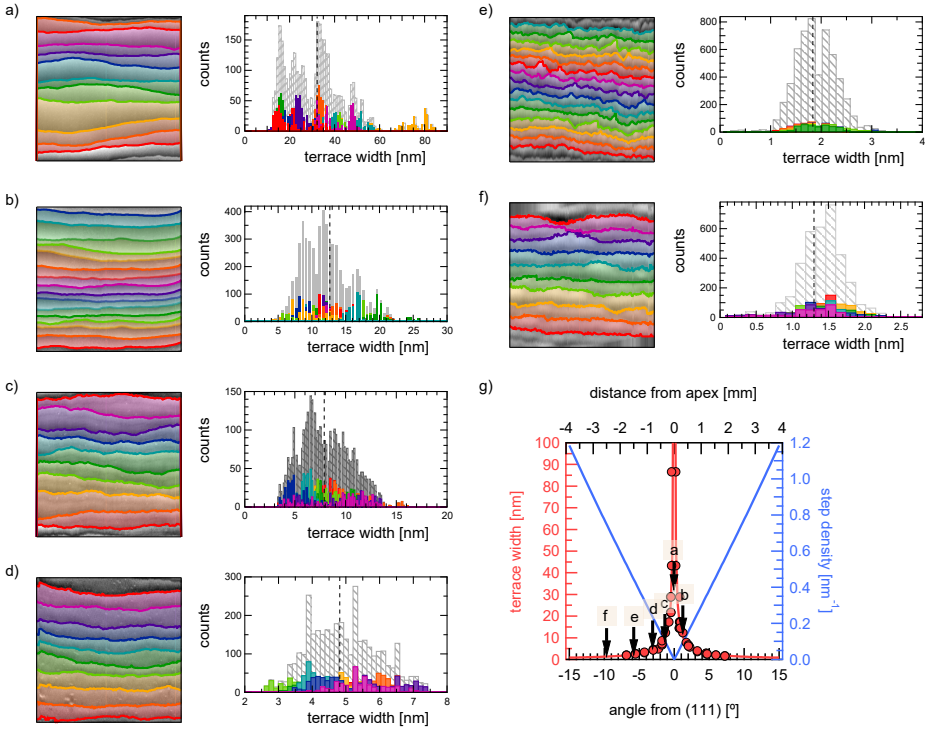

Figure 3.5: Typical STM images from various position along the crystal's curvature, and terrace width distributions for each image. Step edges determined by the analysis procedure and corresponding terraces, are overlaid in colors. The graphs on the right show terrace widths per terrace, as well as summed up (grey bars). Width of each bar in the histograms is 0.1385 nm, i.e. half integer atomic terrace widths. a) Image size: 375×375 nm; mean terrace width ($\tilde{w}$): 32.4 nm. (-0.00785 mm from apex) b) Image size: 300×300 nm; $\tilde{w}$: 12.3 nm. (+0.328 mm from apex) c) Image size: 80×80 nm; $\tilde{w}$: 7.92 nm. (-0.3446 mm from apex) d) Image size: 50×50 nm; $\tilde{w}$: 4.8 nm. (-0.8 mm from apex) e) Image size: 30×30 nm; $\tilde{w}$: 1.8 nm. (-1.5 mm from apex) f) Image size: 15×15 nm; $\tilde{w}$: 1.3 nm. (-2.5 mm from apex) g) Expected mean terrace widths and step densities versus position on the crystal. Black arrows indicate position where a) – f) were obtained.

Generally, surfaces close to the apex feature wide terraces, separated by strongly meandering step edges that may substantially deviate from the direction dictated by our curved crystal's orientation. They sometimes show local fluctuations of step densities that deviate from the expected average step density. For our analysis we can therefore only use data obtained some distance away from the apex, showing terraces in step arrays oriented in the right direction. Figure 3.5 shows typical STM images from different locations across the curved crystal, where regular step arrays were found. Figure 3.5a) shows an STM image of a step array with wide terraces. The mean terrace width ($\tilde{w}$) is 32.4 nm. The step edges as found by the Igor Pro procedure are outlined in different colors. To the right, we plot terrace width histograms per terrace (corresponding color), and the overall distribution (grey bars). The terrace width distribution is very irregular and shows several maxima and shoulders, as well as apparent gaps in the distribution. b) – f) show STM images with increasingly narrow

step arrays and the consequent distributions. They demonstrate how the distributions become first smoother (more continuous) and then more symmetric for higher step densities. Figure 3.5e) also is a good illustration of the kinked nature of the step edges.

While the analysis of individual STM images gives some qualitative insight into the behavior of little and highly stepped surfaces, individual images may not represent the average structure at this miscut angle appropriately. We therefore sum distributions obtained from several STM images with the same average terrace width to obtain histograms with 4600 – 11600 terrace widths included in the data. We normalize counts to a normalized probability. We also increase the bin size to 2 atomic sizes.

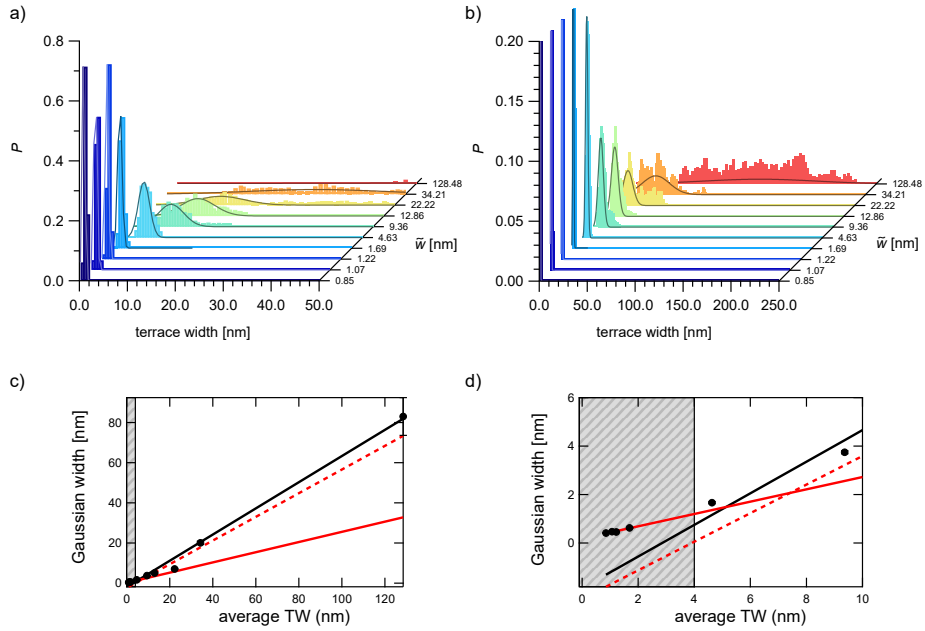

Figure 3.6: a) Normalized terrace width distributions for very narrow and increasingly wide step arrays on the curved Pt crystal with kinked step edges. The mean terrace widths $\tilde{w}$ of the distributions are noted on the right axis. For the 128.5 nm only the onset of the distribution is shown due to the x-axis being limited to 50 nm. Gaussian fits are included and give a good fit for the narrow arrays and deviate from the less symmetric distributions at higher terrace widths. b) Same as a) but showing the x-axis range is extended to 250 nm and y-axis reduced to 0.2, in order to show distributions at higher terrace widths. c) Round markers: $\tilde{w}$ parameter obtained from the Gaussian fits according to equation 3.1 versus mean terrace width of the distributions. Black line: Linear fit to all points. Red solid line: linear fit to the first 4 data points (TW < 4 nm). Red dashed line: Linear fit to the remaining 5 data points (TW > 4 nm). d) Zoom-in of Graph in c), to show data in fits in the range 0 – 10 nm.

We then obtain the distributions in figure 3.6 for statistical analysis. Figures 3.6a) and b) show the terrace width distributions used for analysis. For distributions with $\tilde{w} < 2$ nm, the distributions have a very narrow and symmetric shape. For distributions with $\tilde{w} > 4$ nm, instead of a symmetric shape, the distributions feature a steep onset before reaching their maximum and develop extensive tails. Similar tails were

observed for stepped Pt surfaces with straight steps by Walter *et al.*[47] However, for the very broad distributions, tails here seem to develop rather into a second peak, as the data from $\tilde{w} > 20$ nm demonstrates. This behavior, as discussed in regards to the individual distributions in figure 3.5, does not average out in the summed and normalised distributions here (figure 3.6b)). This indicates a inherent preference for introducing wider terraces into the regular arrays. Both LEED and STM confirm that these wider terraces are not caused by step doubling. For the widest set, it cannot be clearly distinguished what the main peak is. The distributions were fitted with a Gaussian distribution with y_0 fixed at 0:

$$f(x) = y_0 + A \cdot e^{-(\frac{x-x_0}{width})^2} \tag{3.1}$$

The resulting Gaussian fits match the distributions at small $\tilde{w}$ well. The distributions at wider terrace widths are not well described by Gaussian functions. It should be noted, that even though the wider distributions can be fitted with functions containing two or more Gaussian distributions, that the center positions of these Gaussians are unique to each distribution. In other words, no common fitting function can be defined using a set of Gaussians with fixed centers. The development of shoulders and second peaks in these distributions therefore do not indicate shared 'magic' terrace width sizes, as were found for vicinal Ag surfaces with the same kinked step-type.[22] As discussed before, Pt has no clear *sp*-surface state, making such clear quantum confinement effects unlikely.

We further analyze the Gaussian fits by plotting the *width* parameters for the fits in figures 3.6c) and d). In c), the entire range of terrace width over which we have analyzed distributions is shown, from a mean terrace width of 0.85 nm to a mean of 128.5 nm. The width parameter of the Gaussian fit increases with terrace width. A linear fit to the entire set of data (black line) agrees reasonably well and yields a slope of ~ 0.65. However, careful examination of the data in figure 3.6d) shows that the fit does not fit data below 10 nm well.

In an earlier study investigating step-step interactions on Pt surfaces with straight (A- or B-type) steps, the authors compared gaussian width to mean terrace width in a similar way as figure 3.6d).[47] There, a steeper increase of Gaussian width with terrace width was found at surfaces with a mean > 4.2 nm. This change was attributed as a transition from a regime governed by elastic interaction to a regime governed by entropic repulsion. While in the elastic regime the steps' dipoles interact with a constant strength, in the wider arrays steps behave as one-dimensional, non-interacting fermions.

The poor fit in figure 3.6d) suggests a similar behavior here. Fitting data from distributions with $\tilde{w}$<4 nm gives a trend line (solid red line) with a much smaller slope (~0.25) than the previous fit over the entire range, in line with the well-ordered step arrays and narrow terrace width distributions in this regime. This slope lies in be-

tween the ones found in the previous study for vicinal surfaces with close-packed steps in the elastic (~0.21) and entropic regime (~0.32).[47] A fit including data of 4 nm<$\tilde{w}$>40 nm (dashed red line), yield a much steeper slope (~0.59). Even though the data $\tilde{w}$>100 nm was excluded, this fit agrees well with the previous fit over the entire range (black line).

The drastic differences found here may be caused by a transition from elastic to entropic interactions dominating the step-step interactions. However, future work including more data around the terrace width of ~5 nm is required to elucidate the transition.

3.4.3. SUMMARY

In summary, while the average step density, as confirmed by LEED and STM behaves as expected across the *c*-Pt(111)[11$\bar{2}$]-31° crystal, we observe clear local fluctuations in the terrace width distributions. This fact may have to be taken into account when observing chemical reactions involving diffusion on the different surfaces. A more detailed STM study, including additional images at terrace widths around 2-10 nm and analysis of their terrace width fluctuations, may reveal insights into the underlying step-step interactions in the future.

3.5. DETERMINING THE STEP CHIRALITY[2]

While the orientation of step edges on the curved sample as confirmed by LEED generates chiral step edges as outlined in 3.2, it is not determined which side of the surface features which chirality. We use the morphology of vacancy islands on the cleaned surface to identify the chirality of the step edges.

The cleaning procedure for the curved Pt crystal as described in chapters 4 and 5 involves a sputtering step, followed by annealing in oxygen and subsequently in vacuum. The last cycle of our cleaning procedure before our STM study however consists of a modified sputter-anneal cycle to avoid high-temperature induced facetting. For the STM study, the final cleaning cycle consists of sputtering at 570 K, and annealing in vacuum at 770 K. See chapter 5 for a thorough discussion of the procedure. During STM imaging we observe that this final cleaning cycle can lead to the presence of vacancy islands that are a single atom layer deep if the annealing time was too short to completely restore the pristine surface after sputtering. These islands, as shown in figure 3.7, feature six flat edges joined by sharp inner corners. The edges follow the direction of straight A- or B-type steps on the (111) terraces. However, the six edges are not of equal lengths and instead alternate between shorter and longer segments.

[2]Parts of this section are included in: T. Roorda, S. V. Auras, and L.B.F. Juurlink. Chiral Surface Characterisation and Reactivity Toward H–D Exchange of a Curved Platinum Crystal. *Topics in Catalysis*, **59**, 1558-1568 (2020).

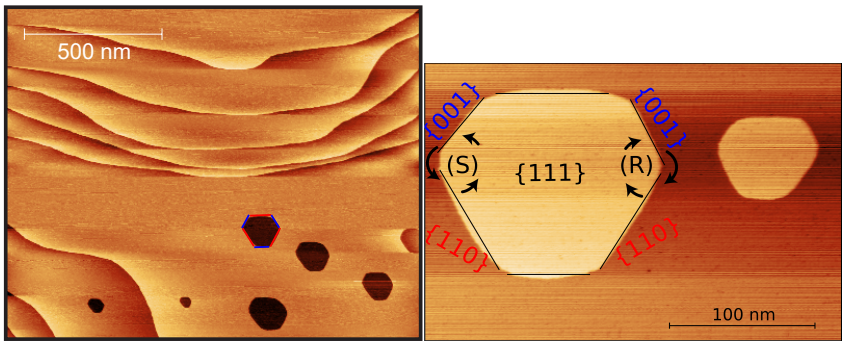

(a) (b)

Figure 3.7: STM images of the surface close to the (111), 80 μm from the approximated apex. After sputtering a short annealing step at 900 K leaves vacancy islands on the surface. Their shape is determined by the line free energies of the two straight step types on the (111) terraces. Segments corresponding to {110}(red) and {001}(blue) microfacets are marked on the vacancy in the center of the STM image.

Figure 3.7 exemplifies the vacancy islands found on the surface close to the apex. In all STM images we only find vacancy islands that are a single atomic layer deep, indicating that during our last sputter step at elevated temperature, the surface is strictly in a layer-by-layer removal regime. The subsequent, final annealing step at 773 K, is carried out at a temperature where vacancy islands on Pt(111) can assume their thermally equilibrated shape.[48] Clearly, the annealing time was not sufficient for all vacancies to be removed. The equilibrium shape can be determined as the Wulff construction of {001} and {110} facets. The length ratio between short and long edges (at equilibrium) then correlates to the line free energy of A- and B-type steps, as shown by Michely *et al.*[48] We have analysed 20 different vacancy islands at 10 locations close to the crystal's apex. The average ratio of long-to-short edge was determined as 0.65 ± 0.06. This agrees very well with the value obtained by Michely et. al at a similar annealing temperature. Since {110}/B-type steps are energetically favored,[49] we can identify the longer step edges as B-type steps and shorter edges as A-type steps.

All of the many vacancy islands appearing in our STM images have the same relative orientation. In combination with the identification of step types forming these islands, we can determine the chirality of stepped surfaces on either side of the crystal. First, we identify the chirality of the corners inside the vacancy islands. We then realize that the left side of a vacancy island reflects the steps on the right side of the curved crystal and vice versa. In figure 3.7, the short edges are marked, in blue, with {001} and the long edge with {110}, in red. We notice that the right corner of the vacancy island, which steps down towards the left, has a clockwise rotational chirality, denoted (*R*). Vice versa, in the left corner we observe a counter-clockwise chirality denoted by (*S*), stepping down towards the right of the crystal. The inherent vacancy defects near the (111) apex of our crystal thus enables us to determine the chirality of the crystal's sides, opening the possibility for controlled chiral adsorption

and reactivity experiments.

3.6. STRUCTURE OF THE KINKED STEP EDGES

3.6.1. MICROSCOPIC RECONSTRUCTIONS ALONG THE KINKED STEP

Figure 3.4 shows the kinked step edges in their fully-kinked form as obtained by the ideal bulk determination. However, the step edge may reconstruct into longer segments with a lower kink density while maintaining its overall orientation, as illustrated in figure 3.8. All possible configurations along this directions are described as energetically equivalent in the Ising model, which describes surfaces in terms of nearest-neighbor interactions.[44] Moreover, the process of reconstruction within a step edge may be influenced by the prevailing step-step interactions between steps, as well as the line free-energies of the microfacets that form the segments in between kinks.

In the limit of complete reconstruction, the entire step could facet into A- and B-type steps separated by a very low density of kink sites. In the two extreme cases, fully-kinked and fully-reconstructed step edges, very different physical and chemical properties may be expected. It is therefore necessary to analyze the structure of the kinked vicinal surfaces along the crystal's curvature before drawing conclusions about the experimentally observed results.

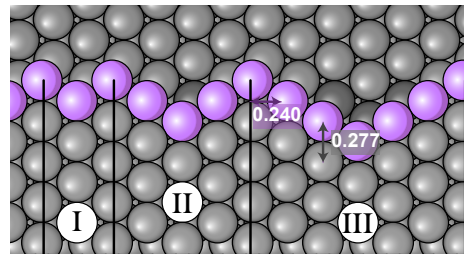

Figure 3.8: The fully-kinked step edge can reconstruct into longer facets while maintaining its overall orientation. I, II, and III show segments with one, two, and three atom wide {001} and {110} microfacets. The distance between atom rows, i.e the atomic spacing along the step edge, is indicated with the purple arrow and is 0.240 nm for Pt. The distance between atoms within a row, indicated by the grey arrow, is the nearest neighbour spacing, 0.277 nm for Pt.

3.6.2. STATISTICAL ANALYSIS OF THE KINKED STEP STRUCTURE

For a suitable set of STM images, where 1 px <1 atom=0.24 nm along the step, we analyse the size of microfacet segments along the step edge. We find the outline of the step with the same procedure as described above. Figure 3.9a) illustrates this. We then determine individual segments by following the step edge (in figure a) along the

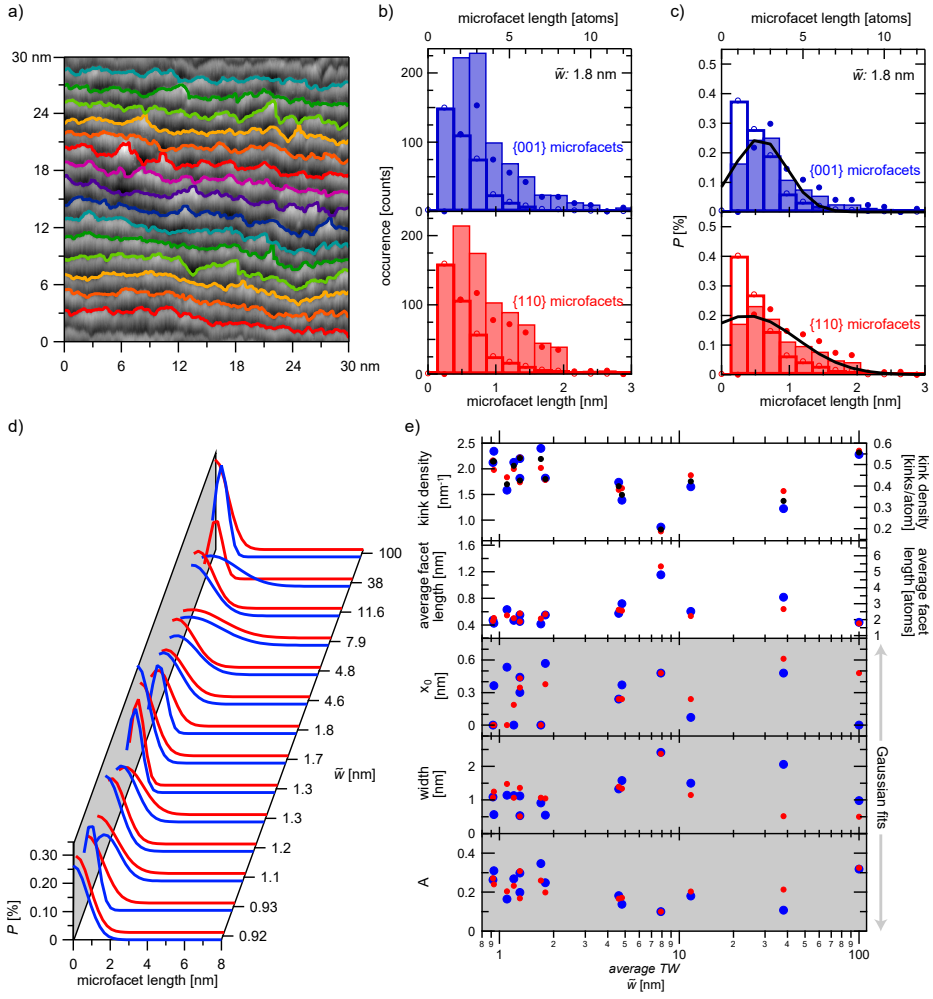

Figure 3.9: a) Example of an STM image (10×10 nm) used for the analysis of corrugation along the kinked step edges. Step edges as found by the Igor Pro procedure are marked in colour. As expected, a high density of kinks separates short segments with varying lengths. b) Distribution of segment lengths along all step edges marked in a), separated for {001} (blue) and {110} (red) facets. Each bin represents an additional atom along the segment length. Bars with thick outlines represent the absolute *number of segments* with a specific length. Filled bars represent the absolute *number of atoms* found in segments of a specific length. Empty circles indicate the cumulative number of (inner and outer) kinks found in segments of each length, filled circles indicate the number of atoms that are not directly at a kink site. c) Normalized distributions of segments, atoms, kink sites, and non-kink atoms in the image. d) Gaussian fits of the normalized distributions of atoms (filled bars in c) in segments of different lengths, for several images along the curvature of the crystal, with average terrace widths $\bar{w}$ ranging from <1 nm to >100 nm. Separate fits were carried out for distributions of {001} (blue) and {110} (red) microfacets. The complete set of distributions included in the analysis can be found in Appendix A. Details of the fitting protocol are explained in the main text. e) Top: kink densities and average facet lengths of the kinked step edges as derived directly from the distribution. (Blue and red markers represent kink densities/ facet lengths in {001} and {110} distributions respectively, black in the entire step.) Bottom: Variable fit parameters of Gaussian fits. While some variation of the parameters is obvious, no clear variation with terrace width or microfacet type is found.

horizontal direction) until its vertical direction (going "up" or "down") reverses for l>0.24 nm. As we have previously determined the step chirality at the two sides of the crystal, we can allocate which segments are {001} and {110} microfacets. We subsequently obtain distributions of microfacet lengths for each type per image in bins of 1 atom row spacing, see figure 3.9b). There, the first bin represents segments with one atom width, i.e. only inner and outer kinks, the second bin contains two atom wide segments, i.e. inner and outer kink atoms separated by one additional atom, etc. Therefore, we can also determine the total number of atoms that can be found in segments of each type, per image. In figure 3.9b), the empty bars with a thick outline show the number of segments of each type. Filled bars with a thin outline give the total number of atoms in segments of each type. Similarly, we can plot the total number of (inner and outer) kink atoms found in segments of each type (empty circles in the figure), and the total number of atoms that are not directly at the kink site (filled circles). For all analyzed images (see also Appendix A) we find the largest number of atoms within the first three bins, i.e. short segments are preferred. This can be explained by simple statistics, where larger deviations from the fully-kinked case have decreasing statistical weight.[44] The distributions in b) make it possible to obtain kink densities and average segment lengths for both types of microfacets. We find these values for kinked step edges in arrays ranging from average terrace widths $\tilde{w}$<1 nm to $\tilde{w}$>100 nm. While there is some variation in the kink densities found in different images, no clear trend is observed. Kink density values, displayed in figure 3.9e) lie consistently in between 1.5 and 2.5 nm^{-1}, corresponding to on average 1.7 - 2.8 atom wide segments along the kinked step edge. For a vicinal Ag surface with $\tilde{w}$ = 1.13 nm, an average length of kinked segments of 2 - 3 atoms has recently observed.[22]

It may be argued that kink densities at step arrays with $\tilde{w}$<2 nm are slightly elevated compared to arrays of larger terrace widths. However, this may also be a consequence of image sizes and consequent resolution at broader terraces; typically images at lower step densities need to be larger to show arrays of multiple steps. An exception to this is the data at $\tilde{w}$>100 nm. There, the mean terrace width was determined from large image that included multiple steps, whereas the kink density distributions were determined from a zoom-in on a single step to achieve the required resolution. The step-step interactions in the arrays of varying step densities thus do not appear to significantly influence the faceting of the kinked step edges.

The overall orientation of the kinked step dictates equal average kink densities for the {001} and {110}-type segments. This is confirmed in figure 3.9e), where kink densities of {001} (blue) and {110} (red) segments are similar for all images. Neither segment type has consistently lower kink densities than the other.

The difference in line free energies, however, may cause different distributions of the

two types. As the number of steps and atoms per image will depend on its size and local step density on the curved crystal, we normalize the distributions (of segments, atoms, kink atoms, non-kink atoms) individually, as demonstrated in figure 3.9c). We then fit the distributions of atoms (filled bars in figures b) and c)) with a Gaussian (see equation 3.1), where $y_0 = 0$ and x_0 is fixed to the x-value of the maximum of the distribution. Distributions for {001} and {110} segments are fitted separately for each analyzed image. All resulting Gaussian fits are displayed in figure 3.9d). Again, some fluctuations are observed, but no clear trend in the width of the Gaussian fits for different microfacet types, nor consistent changes with terrace width $\tilde{w}$. The fitting parameters as plotted in figure 3.9e), reflect this. We attribute variations in the fits to the limited amount of data available to the distributions (about 90 - 600 per distribution), resulting from the image size and steps in each image. We expect these distributions to become even more uniform if more images at the same $\tilde{w}$ would be analyzed.

The line-free energy of longer segments, which varies for A- and B-type steps does not appear to significantly influence the structure of the kinked step edges. This suggests a larger influence of the kink energy, as well as entropy.

3.6.3. SUMMARY

Detailed analysis of the {210} step edges allows us to atomically resolve the roughening of the step edge into segments of variable length. Only a fraction of the atoms along the kinked step edges are in fully-kinked, one atom wide, segments. However, reconstructions into very large segments that may behave as A-or B-type steps are statistically not favored. Furthermore, the different atomic arrangements of {001} or {110}-oriented segments do not lead to different distributions. Across the *c*-Pt(111)[11$\bar{2}$]-31° crystal, no consistent changes of kink densities or distributions of segment length with average terrace width are observed. We thus conclude that the atomic structure of the kinked step edges is similar for all surface structures contained on the crystal.

REFERENCES

[1] J. Wintterlin, S. Völkening, T. V. Janssens, T. Zambelli, and G. Ertl. Atomic and macroscopic reaction rates of a surface-catalyzed reaction. *Science*, 278(5345):1931–1934, 1997.

[2] H. Ueta and M. Kurahashi. Steric effect in CO oxidation on Pt(111). *Journal of Chemical Physics*, 147(19), 2017.

[3] H. J. Freund, G. Meijer, M. Scheffler, R. Schlögl, and M. Wolf. CO oxidation as a

prototypical reaction for heterogeneous processes. *Angewandte Chemie - International Edition*, 50(43):10064–10094, 2011.

[4] D. L. Bashlakov, L. B. Juurlink, M. T. Koper, and A. I. Yanson. Subsurface oxygen on Pt(111) and its reactivity for CO oxidation. *Catalysis Letters*, 142(1):1–6, 2012.

[5] G. J. Kroes and C. Díaz. Quantum and classical dynamics of reactive scattering of H_2 from metal surfaces. *Chemical Society Reviews*, 45(13):3658–3700, 2016.

[6] M. K. Sabbe, M. F. Reyniers, and K. Reuter. First-principles kinetic modeling in heterogeneous catalysis: An industrial perspective on best-practice, gaps and needs. *Catalysis Science and Technology*, 2(10):2010–2024, 2012.

[7] J. Neugebohren, D. Borodin, H. W. Hahn, J. Altschäffel, A. Kandratsenka, D. J. Auerbach, C. T. Campbell, D. Schwarzer, D. J. Harding, A. M. Wodtke, and T. N. Kitsopoulos. Velocity-resolved kinetics of site-specific carbon monoxide oxidation on platinum surfaces. *Nature*, 558(7709):280–283, 2018.

[8] L. Zhou, A. Kandratsenka, C. T. Campbell, A. M. Wodtke, and H. Guo. Origin of Thermal and Hyperthermal CO_2 from CO Oxidation on Pt Surfaces: The Role of Post-Transition-State Dynamics, Active Sites, and Chemisorbed CO2 . *Angewandte Chemie*, 131(21):6990–6994, 2019.

[9] A. Gutiérrez-González, M. E. Torio, H. F. Busnengo, and R. D. Beck. Site Selective Detection of Methane Dissociation on Stepped Pt Surfaces. *Topics in Catalysis*, 62(12-16):859–873, 2019.

[10] H. Chadwick, A. Gutiérrez-González, D. Migliorini, R. D. Beck, and G. J. Kroes. Incident Angle Dependence of CHD_3 Dissociation on the Stepped Pt(211) Surface. *Journal of Physical Chemistry C*, 122(34):19652–19660, 2018.

[11] H. Chadwick, A. Gutiérrez-González, R. D. Beck, and G. J. Kroes. Transferability of the SRP32-vdW specific reaction parameter functional to CHD_3 dissociation on Pt(110)-(2 × 1). *Journal of Chemical Physics*, 150(12), 2019.

[12] F. Garcia-Martinez, C. García-Fernández, J. P. Simonovis, A. Hunt, A. Walter, I. Waluyo, F. Bertram, L. R. Merte, M. Shipilin, S. Pfaff, S. Blomberg, J. Zetterberg, J. Gustafson, E. Lundgren, D. Sánchez-Portal, F. Schiller, and J. E. Ortega. Catalytic Oxidation of CO on a Curved Pt(111) Surface: Simultaneous Ignition at All Facets through a Transient CO-O Complex. *Angewandte Chemie - International Edition*, 2020.

[13] R. Van Lent, S. V. Auras, K. Cao, A. J. Walsh, M. A. Gleeson, and L. B. Juurlink. Site-specific reactivity of molecules with surface defects—the case of H_2 dissociation on Pt. *Science*, 363(6423):155–157, 2019.

[14] S. V. Auras, R. van Lent, D. Bashlakov, J. M. Piñeiros Bastidas, T. Roorda, R. Spierenburg, and L. B. Juurlink. Scaling Platinum-Catalyzed Hydrogen Dissociation on Corrugated Surfaces. *Angewandte Chemie - International Edition*, 2020.

[15] C. J. Bondue, F. Calle-Vallejo, M. C. Figueiredo, and M. T. Koper. Structural principles to steer the selectivity of the electrocatalytic reduction of aliphatic ketones on platinum. *Nature Catalysis*, 2(3):243–250, 2019.

[16] I. T. McCrum, X. Chen, K. A. Schwarz, M. J. Janik, and M. T. Koper. Effect of Step Density and Orientation on the Apparent pH Dependence of Hydrogen and Hydroxide Adsorption on Stepped Platinum Surfaces. *Journal of Physical Chemistry C*, 122(29):16756–16764, 2018.

[17] K. Honkala, A. Hellman, I. N. Remediakis, A. Logadottir, A. Carlsson, S. Dahl, C. H. Christensen, and J. K. Nørskov. Ammonia Synthesis from First-Principles Calculations. *Science*, 307(5709):555–558, 2005.

[18] G. Sun and P. Sautet. Metastable Structures in Cluster Catalysis from First-Principles: Structural Ensemble in Reaction Conditions and Metastability Triggered Reactivity. *Journal of the American Chemical Society*, 140(8):2812–2820, 2018.

[19] G. Sun, A. N. Alexandrova, and P. Sautet. Pt8 cluster on alumina under a pressure of hydrogen: Support-dependent reconstruction from first-principles global optimization. *Journal of Chemical Physics*, 151(19), 2019.

[20] H. Chadwick, A. Gutiérrez-González, R. D. Beck, and G. J. Kroes. CHD3 Dissociation on the Kinked Pt(210) Surface: A Comparison of Experiment and Theory. *Journal of Physical Chemistry C*, 123(23):14530–14539, 2019.

[21] S. M. Davis and G. A. Somorjai. The effect of surface oxygen on hydrocarbon reactions catalyzed by platinum crystal surfaces with variable kink concentrations. *Surface Science*, 91(1):73–91, 1980.

[22] J. E. Ortega, G. Vasseur, I. Piquero-Zulaica, S. Matencio, M. A. Valbuena, J. E. Rault, F. Schiller, M. Corso, A. Mugarza, and J. Lobo-Checa. Structure and electronic states of vicinal Ag(111) surfaces with densely kinked steps. *New Journal of Physics*, 20(7), 2018.

[23] M. Giesen and S. Dieluweit. Step dynamics and step-step interactions on the chiral Cu(5 8 90) surface. *Journal of Molecular Catalysis A: Chemical*, 216(2):263–272, 2004.

[24] J. Frohn, M. Giesen, M. Poensgen, J. F. Wolf, and H. Ibach. Attractive interaction between steps. *Physical Review Letters*, 67(25):3543–3546, 1991.

[25] N. C. Bartelt, T. L. Einstein, and E. D. Williams. The influence of step-step interactions on step wandering. *Surface Science*, 240:L591–L598, 1990.

[26] J. L. Gland, M. R. McClellan, and F. R. McFeely. Carbon monoxide oxidation on the kinked Pt(321) surface. *The Journal of Chemical Physics*, 79(12):6349–6356, 1983.

[27] A. D. Smeltz, W. N. Delgass, and F. H. Ribeiro. Oxidation of NO with O_2 on Pt(111) and Pt(321) large single crystals. *Langmuir*, 26(21):16578–16588, 2010.

[28] A. J. Gellman, J. D. Horvath, and M. T. Buelow. Chiral single crystal surface chemistry. *Journal of Molecular Catalysis A: Chemical*, 167(1-2):3–11, 2001.

[29] A. J. Gellman, Y. Huang, A. J. Koritnik, and J. D. Horvath. Structure-sensitive enantiospecific adsorption on naturally chiral Cu(hkl)$^{R\&S}$ surfaces. *Journal of Physics Condensed Matter*, 29(3), 2017.

[30] J. D. Horvath and A. J. Gellman. Enantiospecific desorption of chiral compounds from chiral Cu(643) and achiral Cu(111) surfaces. *Journal of the American Chemical Society*, 124(10):2384–2392, 2002.

[31] J. D. Horvath, A. Koritnik, P. Kamakoti, D. S. Sholl, and A. J. Gellman. Enantioselective separation on a naturally chiral surface. *Journal of the American Chemical Society*, 126(45):14988–14994, 2004.

[32] Y. Yun and A. J. Gellman. Enantioselective separation on naturally chiral metal surfaces: D,L-aspartic acid on Cu(3,1,17)$^{R\&S}$ surfaces. *Angewandte Chemie - International Edition*, 52(12):3394–3397, 2013.

[33] D. S. Wei, B. S. Mhatre, A. J. Gellman, and D. S. Sholl. Contributions of dispersion forces to R-3-methylcyclohexanone physisorption on low and high Miller index Cu surfaces. *Surface Science*, 629:35–40, 2014.

[34] Y. Yun and A. J. Gellman. Enantiospecific Adsorption of Amino Acids on Naturally Chiral Cu{3,1,17}$^{R\&S}$ Surfaces. *Langmuir*, 31(22):6055–6063, 2015.

[35] A. D. Reinicker, A. J. Therrien, T. J. Lawton, R. Ali, E. C. Sykes, and A. J. Gellman. Influence of step faceting on the enantiospecific decomposition of aspartic acid on chiral Cu surfaces vicinal to Cu{111}. *Chemical Communications*, 52(75):11263–11266, 2016.

[36] D. M. Rampulla, A. J. Francis, K. S. Knight, and A. J. Gellman. Enantioselective surface chemistry of R-2-bromobutane on Cu(643)$^{R\&S}$ and Cu(531)$^{R\&S}$. *Journal of Physical Chemistry B*, 110(21):10411–10420, 2006.

[37] D. S. Sholl. Adsorption of chiral hydrocarbons on chiral platinum surfaces. *Langmuir*, 14(4):862–867, 1998.

[38] T. D. Power, A. Asthagiri, and D. S. Sholl. Atomically detailed models of the effect of thermal roughening on the enantiospecificity of naturally chiral platinum surfaces. *Langmuir*, 18(9):3737–3748, 2002.

[39] D. S. Sholl, A. Asthagiri, and T. D. Power. Naturally chiral metal surfaces as enantiospecific adsorbents. *Journal of Physical Chemistry B*, 105(21):4771–4782, 2002.

[40] G. A. Attard. Electrochemical studies of enantioselectivity at chiral metal surfaces. *Journal of Physical Chemistry B*, 105(16):3158–3167, 2001.

[41] A. Ahmadi, G. Attard, J. Feliu, and A. Rodes. Surface reactivity at 'chiral' platinum surfaces. *Langmuir*, 15(7):2420–2424, 1999.

[42] G. A. Attard, A. Ahmadi, J. Feliu, A. Rodes, E. Herrero, S. Blais, and G. Jerkiewicz. Temperature effects in the enantiomeric electro-oxidation of D- and L-glucose on Pt{643}^{S}. *Journal of Physical Chemistry B*, 103(9):1381–1385, 1999.

[43] P. W. Palmberg, G. Riach, R. Weber, and N. MacDonald. *Handbook of Auger Electron Spectroscopy*. Physical Electronics Industries Inc., Edina, 1 edition, 1972.

[44] H. Ibach. *Physics of surfaces and interfaces*. 2006.

[45] P. Roos, E. Bertel, and K. D. Rendulic. Observation of an sp-derived surface resonance on Pt(111) indicating the crucial role of surface states in physisorption. *Chemical Physics Letters*, 232(5-6):537–541, 1995.

[46] G. Fischer and H. Hoffman. Oscillations of the electrical conductivity with film thickness in very thin platinum films. *Solid State Communications*, 35(10):793–796, 1980.

[47] A. L. Walter, F. Schiller, M. Corso, L. R. Merte, F. Bertram, J. Lobo-Checa, M. Shipilin, J. Gustafson, E. Lundgren, A. X. Brión-Ríos, P. Cabrera-Sanfelix, D. Sánchez-Portal, and J. E. Ortega. X-ray photoemission analysis of clean and carbon monoxide-chemisorbed platinum(111) stepped surfaces using a curved crystal. *Nature Communications*, 6:1–7, 2015.

[48] T. Michely and G. Comsa. Temperature dependence of the sputtering morphology of Pt(111). *Surface Science*, 256(3):217–226, 1991.

[49] A. M. Lahee, J. R. Manson, J. P. Toennies, and C. Wöll. Observation of Interference Oscillations in Helium Scattering from Single Surface Defects. *Physical Review Letters*, 57(18):2331–2331, 1986.